



Research Article

Investigation of the Effects of an Inferior Vena Cava Filter and Captured Clot Size on the Hemodynamic Parameters in Non-Newtonian Turbulent Pulsatile Blood Flow

Jafar Moradicheghamahi ¹, Muhammad Qasim ¹, Sohrab Jafarpour ², and Hamed Farokhi ²

¹Departament d'Enginyeria Informàtica i Matemàtiques, Universitat Rovira i Virgili, Tarragona, Spain

²Department of Mechanical and Construction Engineering, Northumbria University, Newcastle upon Tyne NE1 8ST, UK

Correspondence should be addressed to Jafar Moradicheghamahi; jafar.moradicheghamahi@urv.cat

Received 23 March 2023; Revised 28 September 2023; Accepted 16 October 2023; Published 31 October 2023

Academic Editor: Qiguo Rong

Copyright © 2023 Jafar Moradicheghamahi et al. This is an open access article distributed under the Creative Commons Attribution License, which permits unrestricted use, distribution, and reproduction in any medium, provided the original work is properly cited.

In this computational fluid dynamics (CFD)-based study, the effects of inferior vena cava (IVC) filter implantation on the risk of IVC thrombosis have been investigated using different hemodynamic parameters, including time-averaged wall shear stress (TAWSS), the oscillating shear index (OSI), and the relative residence time (RRT). The boundary conditions in this study have been based on physiological pulses. Additionally, the $k-\omega$ model and the Carreau model have been chosen to represent the turbulent flow regime and non-Newtonian blood, respectively. For this purpose, three blood clots with the largest cross-sectional diameters of 30%, 50%, and 70% of the filter diameter have been used. Capturing a small clot in the filter has the minimum effect on the hemodynamic parameters, while by increasing the size of the captured clot, OSI and RRT parameters increase in areas downstream of the filter on the wall. The presence of a filter and clot increases the risk of thrombosis. In the case of capturing large clots, there is the possibility of damage to endothelial cells or platelet activation. Captured clots lead to the formation of plaque and thrombus on the IVC wall. However, the possibility of thrombus growth on its surface is not negligible, particularly if larger clots are trapped in the filter.

1. Introduction

Pulmonary embolism (PE) is the third highest cause of mortality from cardiovascular diseases, following heart attack and stroke [1]. PE, mostly due to deep vein thrombosis (DVT), occurs when a venous thrombus is embolized and reaches the pulmonary arteries through inferior vena cava (IVC). PE can impair oxygen delivery, put strain on the heart, or even lead to death [2].

Implanting an IVC filter is a suitable option to catch emboli in the pulmonary circulation in particular situations, such as severe bleeding that prevents the use of anticoagulants [3]. IVC filters are metal devices that help prevent PE by trapping thrombi traveling through the blood flow and preventing them from entering the lungs [4].

The effectiveness of the IVC filter is difficult to interpret based on clinical reports alone [5]. The positive impact of these filters has been much debated. In some clinical studies performed on patients, the positive effect of these filters has been emphasized [6]. In some other clinical studies, the implantation of these filters has been reported to be ineffective in patients taking anticoagulants [7].

When compared to in vitro and in vivo studies, computational fluid dynamics (CFD) makes it easier to calculate hemodynamic parameters such as time-averaged wall shear stress (TAWSS), oscillating shear index (OSI), and relative residence time (RRT) with high accuracy [8, 9]. As has been shown in numerous in vitro [5, 10, 11] and computational studies [12–14], a deep understanding of hemodynamics effectively determines IVC filters' advantages and disadvantages.

One of filter implants' most common side effects is thrombosis [15, 16]. A 2005 clinical study reported a rise in DVT in the years after IVC filter implantation, most likely due to caval occlusion due to the filter [16]. Numerous studies have been performed on IVC thrombosis, which is the subject of this study. In all these studies, the effect of filter and emboli on the occurrence of IVC thrombosis has been predicted by analyzing the flow patterns and shear stress around the filter.

Areas with stagnant or reverse flow and low velocity are generally prone to thrombosis [17]. Studies of blood flow around a filter with a captured clot have found stagnant or recirculation regions downstream of the clot that may increase the risk of thrombosis [5, 10, 11]. It has been shown that partial occlusion of a vein by the presence of clots results in regions with a recirculating flow [14, 18] or turbulent flow [5, 19–21] that are prone to thrombosis. Studies have shown that the presence of an IVC filter without any captured clot does not have much effect on blood flow [3]. In the unoccluded filter condition, the turbulence intensity is minimal, and the only area where a small amount of turbulence is observed is near the apex [5]. In addition to areas with low wall shear stress (WSS), regions with high WSS (5–10 Pa) can also be thrombogenic due to their effect on certain cellular signaling processes [22].

The intensity of turbulence or stagnation of the flow depends not only on the size of the clot but also on the slant angle of the clot. In clots with more drastic slant angles and shorter cones, flow turbulence and flow recirculation are greater [5]. In most CFD studies, simple models such as spherical models [14, 21] or conical models with spherical ends [3, 19, 23] have been used to model clots. But it has been observed that clots tend to adapt to filter shape [4].

Simplified geometries in the study of IVC hemodynamics are common [24, 25]. However, realistic geometries lead to higher values for pressure drop and WSS compared to simplified models [3]. Consequently, in simulations using simplified geometries such as tubes, a realistic physiological flow pattern cannot be obtained [20]. Therefore, using a realistic geometry in the IVC hemodynamics studies seems necessary.

Blood is composed of plasma, minerals, and red blood cells. The plasma behavior is almost Newtonian, while the red blood cells cause the blood's non-Newtonian behavior. In recent years, numerous studies have been conducted on blood fluid behavior to achieve a suitable model [3, 26–29]. By examining the OSI contour for different rheological models, it has been demonstrated that the Carreau non-Newtonian model has a better prediction for OSI and its maximum value [9]. The Carreau model has been proposed as the most appropriate model for blood in several studies [9, 30, 31], which will also be used in this study.

While veins typically exhibit laminar flow due to their lower velocity, several factors can disrupt local flow patterns, potentially leading to regions of turbulence. The existence of clot in the blood vessel can affect the blood flow [32]. An IVC filter containing large clots, which have the potential to nearly occlude the vein and alter blood flow patterns, thereby inducing flow separation, increased shear stress, and downstream

turbulence, all of which are associated with an elevated risk of thrombosis [19, 33]. It has been observed that transitional zones tend to manifest at least one diameter downstream from these substantial clots [20]. Additionally, turbulent characteristics may emerge at the points where renal veins join the IVC, owing to the flow negotiating bifurcations. Similarly, blood flow can turn turbulent when navigating through stenosed arteries or branching points, a phenomenon that plays a pivotal role in the initiation and formation of plaques [34, 35]. Blood flow itself exhibits a pulsatile nature, rendering it more amenable to modeling as turbulent flow. The turbulence, stemming from erratic fluid motions and temporal, as well as spatial fluctuations in flow direction and rates, contributes significantly to the development of thrombosis [36]. Turbulent blood flow increases the contact time of blood components and endothelial cells, which triggers platelet activity and causes blood lipids to penetrate and accumulate in the intima [37]. Due to the high accuracy in the boundary layers and, thus, in the calculation of hemodynamic parameters, and the low computational cost, in many studies on blood flow, the k - ω model has been used [9, 38, 39].

In this computational study, using hemodynamic parameters in a realistic geometry of IVC, the effect of the filter implantation and blood clots on the exacerbation of IVC thrombosis has been investigated. In previous studies, constant values have been used for inlet velocities and outlet pressure, while in this study, realistic pulsatile boundary conditions have been used for the inlet velocities and the outlet pressure. Another innovation of this research is related to the way of evaluating the areas prone to IVC thrombosis. To our best knowledge, this is the first study that uses TAWSS, OSI, and RRT parameters to evaluate the risk of IVC thrombosis. To have a more precise study of the pulsatile flow in IVC, the k - ω turbulence model for the flow and the Carreau non-Newtonian model for the blood have been used.

2. Methods

2.1. Governing Equations. The incompressible unsteady Reynolds-averaged Navier–Stokes equations that determine fluid motion have the following general form [30, 40, 41]:

$$\frac{\partial \rho}{\partial t} + \frac{\partial}{\partial x_i} (\rho u_i) = 0, \quad (1)$$

$$\begin{aligned} & \frac{\partial}{\partial t} (\rho u_i) + \frac{\partial}{\partial x_j} (\rho u_i u_j) \\ &= -\frac{\partial p}{\partial x_i} + \frac{\partial}{\partial x_j} \left[\mu \left(\frac{\partial u_i}{\partial x_j} + \frac{\partial u_j}{\partial x_i} - \frac{2}{3} \delta_{ij} \frac{\partial u_k}{\partial x_k} \right) \right] + \frac{\partial}{\partial x_j} (-\rho \overline{u_i u_j}) + F_i. \end{aligned} \quad (2)$$

To predict the non-Newtonian fluid behavior of blood, the Carreau model is used [42, 43]:

$$\mu = \mu_\infty + (\mu_0 - \mu_\infty)(1 + A|\dot{\gamma}|^2)^n, \quad (3)$$

where $A = 10.976$, $n = -0.3216$, $\mu_\infty = 0.0035$, and $\mu_0 = 0.056$.

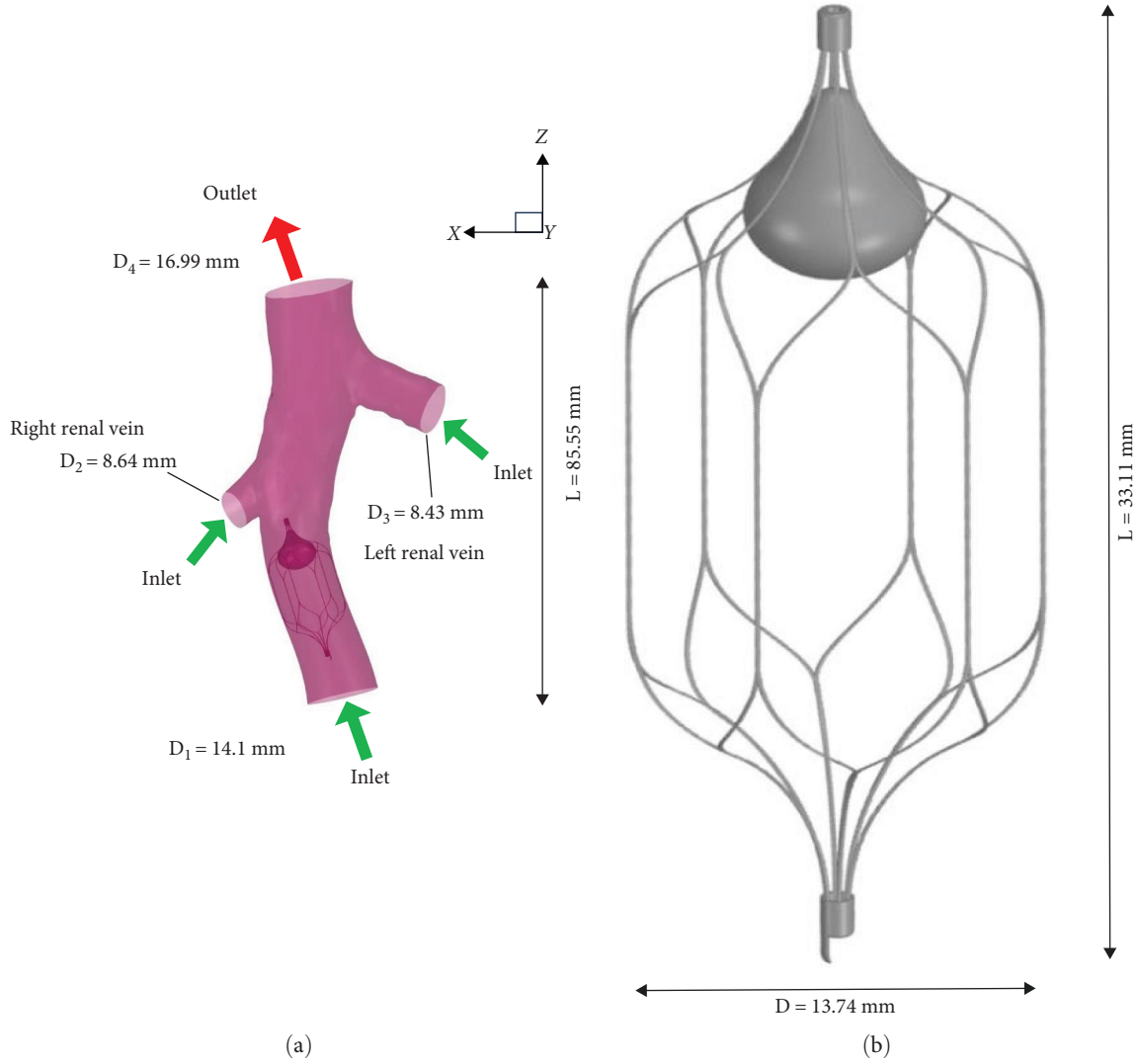


FIGURE 1: (a) Geometry of simulated IVC; (b) geometry of the filter and a medium clot.

The term $\partial/\partial x_j(-\rho\overline{u_i u_j})$ in Equation (2) is omitted for laminar flows. This term is modeled as follows for turbulent flows:

$$\mu_t S^2 = -\rho\overline{u_i u_j} \frac{\partial u_j}{\partial x_i} \text{ with } S = \sqrt{2S_{ij}S_{ij}}, \quad (4)$$

where p is the pressure, S is the mean strain rate tensor's modulus, and μ_t is blood's turbulence viscosity. The value of μ_t in the k - ω turbulence model used in this study is determined as follows:

$$\mu_t = \alpha^* \frac{\rho k}{\omega}, \quad (5)$$

where the low Reynolds number correction is caused by the coefficient α^* , which damps the turbulent viscosity [40]. Equations (6) and (7) calculate the values of k and ω , respectively:

$$\frac{\partial}{\partial t}(\rho k) + \frac{\partial}{\partial x_i}(\rho k u_i) = \frac{\partial}{\partial x_j} \left[\left(\mu + \frac{\mu_t}{\sigma_k} \right) \frac{\partial k}{\partial x_j} \right] + G_k - Y_k + S_k, \quad (6)$$

$$\frac{\partial}{\partial t}(\rho \omega) + \frac{\partial}{\partial x_i}(\rho \omega u_i) = \frac{\partial}{\partial x_j} \left[\left(\mu + \frac{\mu_t}{\sigma_\omega} \right) \frac{\partial \omega}{\partial x_j} \right] + G_\omega - Y_\omega + S_\omega. \quad (7)$$

The parameters and constants used in Equations (5)–(7) are available in a study by Fluent [40].

2.2. Problem Statement. In this study, a 3D realistic geometry of IVC, as shown in Figure 1(a), is used to investigate the hemodynamic parameters in IVC. All dimensions are shown in the figure. This geometry is a part of the IVC to which the renal veins are connected. In addition, this study employs the TrapEase IVC model (Figure 1(b)). This model is in the form of a symmetrical hexagonal basket that provides two areas to

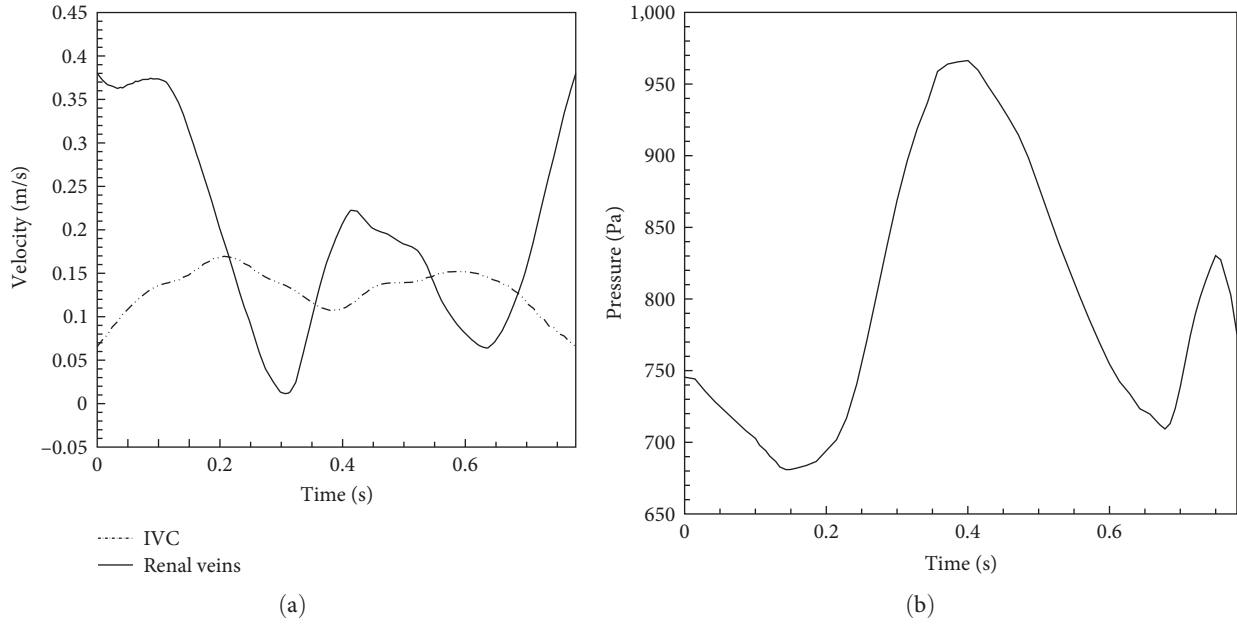


FIGURE 2: (a) Physiological pulses utilized as inlet; (b) outlet boundary conditions.

capture clots. It is essential to emphasize that, during the real placement procedure, the IVC filter is inserted into the vein using a capsule that contains the folded filter. The filter is carefully unfolded at the discretion of the practitioner to ensure proper contact with the IVC wall [44]. In this study, similar to previous research [4, 44], we attempted to optimize filter placement by adjusting its angle and position to enhance contact with the vessel wall. Given the initial geometry derived from CT scan data, there was no location closely resembling an ideal cylindrical shape. Consequently, we utilized SpaceClaim software to make specific modifications to the vein's geometry, creating a configuration that more closely approximated a cylindrical shape around the filter. This alteration promotes increased contact between the filter and the vessel wall, thereby bringing the simulation closer to a realistic scenario compared to previous studies. This study examines three types of blood clots: small, medium, and large blood clots with diameters of 30%, 50%, and 70% of the filter diameter. As mentioned in previous studies [3, 4], the geometry of the clot tends to adapt to the filter geometry.

The physiological pulses used as boundary conditions are shown in Figure 2. These pulses include two velocity pulses for the IVC inlet and the renal veins inlet and a pressure pulse for the IVC outlet [45, 46]. In this study, we modeled the clot within the blood vessel as a fixed, immobile internal rigid wall, consistent with previous computational studies on IVC filters [4, 44, 47]. We chose not to use a multiphase simulation approach and assumed that the clot's position and size remained constant throughout the simulations. This approach allowed us to focus on assessing the effects of the clot and filter on blood flow patterns without considering clot movement or deformation. Additionally, no-slip boundary conditions were applied to all walls.

The finite volume approach was used to numerically solve the governing equations. Two simulations were performed for

meshes with various element sizes to ensure that the results are independent of the number of computational cells. We utilized the Carreau model as the blood non-Newtonian model and the $k-\omega$ model as the turbulent model in this steady-state simulation. Additionally, there was no filter at the vein, and the velocity was set at 0.15 m/s at the inlet and 0.25 m/s at the renal veins. WSS values were extracted and compared for different meshes along a line on the IVC surface (indicated in red in Figure 3(a)). It is evident from the figure that the WSS value has not changed significantly by decreasing the minimum element size to less than $2e-4$ m. After confirming that results on the IVC surface were independent of mesh size, another simulation was run by including a filter with a captured large clot. On the surface of the filter and the clot, the minimum element size of $5e-5$ m was selected, and the values of WSS were evaluated along a line on the clot surface. The simulation was repeated for meshes with smaller element sizes, yielding the same WSS graph (Figure 3(b)). Based on this mesh study, the minimum element sizes used in all simulations were $2e-4$ m on the IVC surface and $5e-5$ m on the filter and clot surface. In both cases, the maximum size of the element was considered to be twice the minimum size of the element.

In the present study, Ansys Fluent Mosaic Meshing has been utilized, which combines the benefits of polyhedral and hexahedral elements to create an efficient and accurate mesh. This technique intelligently assigns polyhedral elements near boundaries to capture complex geometries and ensure boundary layer resolution. Meanwhile, hexahedral elements are used in the core region for improved mesh quality and reduced numerical diffusion [48]. Tetrahedral meshes are commonly used in numerical simulations [49, 50] due to their ease of generation, but they often require high RAM usage and longer computational time [48, 51]. Although hexahedral meshes offer advantages, they are limited to

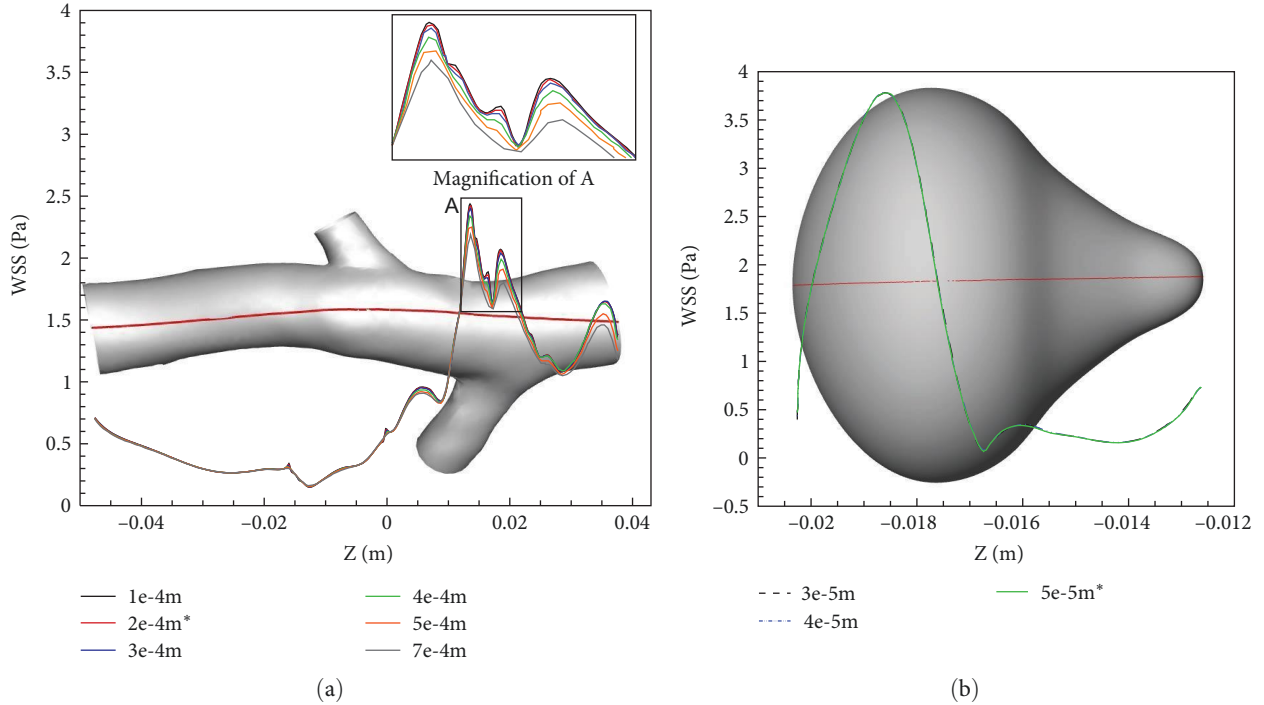


FIGURE 3: Mesh independence study: (a) WSS changes along the red line on the IVC surface for meshes with different element sizes; (b) WSS changes along the red line on the clot surface for meshes with different element sizes.

simple geometries [41, 51–53]. Ansys Fluent Mosaic Meshing overcomes these limitations by providing efficient mesh generation, even for complex geometries, resulting in reduced computational cost and accurate boundary layer resolution. It combines the advantages of both methods without significant drawbacks, making it a favorable choice in numerical simulations [48, 51, 53].

Due to the fact that this type of mesh is new, to ensure its accuracy, the results were compared with the case with meshes made of tetrahedral elements, which are widely used, and the same results were obtained. The details of the selected mesh for the simulations with a large clot are shown in Figure 4.

The commercial CFD software Ansys Fluent 2020 R1 was used for flow visualization and analysis. The equations were discretized using a third-order MUSCL differencing scheme. The coupled method was used for the pressure–velocity correction. The residual error convergence threshold for the momentum equations was set to $1e-6$. According to previous studies [54], unsteady simulations were conducted for three consecutive pulses to eliminate transient effects, and the results were based on the third pulse. The maximum number of iterations per step was set to 40 in all simulations, and the time step was 0.005 s. No meaningful change was found in sensitivity tests using a time step of 0.002 and maximum iterations of 80.

2.3. Validation. The simulation of the base model in the López et al.’s [44] paper was repeated to validate the CFD model used in this study. The density of the blood was $\rho = 1,060 \text{ kg/m}^3$, and the Carreau non-Newtonian model (Equation (3)) was employed in this simulation. The

geometry used for the validation was similar to that used in the current study. However, there were some differences in the vein wall’s dimensions and smoothness; compared to the current model, it was longer (20 cm compared to 15 cm) and had a rougher surface. In addition, the inlet and outlet diameters were larger. This simulation, which was proposed to simulate the blood flow in the IVC under rest conditions, was a steady-state simulation. The inlet flow rate was $20 \text{ cm}^3/\text{s}$, and at the renal veins, it was $7 \text{ cm}^3/\text{s}$. The pressure at the outlet was assumed to be zero. The simulation was run under these conditions, and the distribution of WSS on the vein wall was calculated (Figure 5(b)). As shown in Figure 5, the present model’s prediction of the distribution of WSS (Figure 5(b)) is in good agreement with the model by López et al. [44] (Figure 5(a)).

2.4. Hemodynamic Parameters. To the effect of the IVC filter, three WSS-based hemodynamic parameters, which are the most common in the hemodynamic study of thrombus growth and atherosclerosis [55], were employed in the present study, including TAWSS, OSI, and RRT.

The TAWSS variable is used to calculate the total shear stress on the wall during the whole cardiac cycle. The following equation is used to compute this variable, which has been employed by earlier studies [9].

$$\text{TAWSS} = \frac{1}{T} \int_0^T |\tau_s| dt. \quad (8)$$

The endothelial cells are continuously subjected to various shear stresses during a cardiac cycle. The OSI is used to

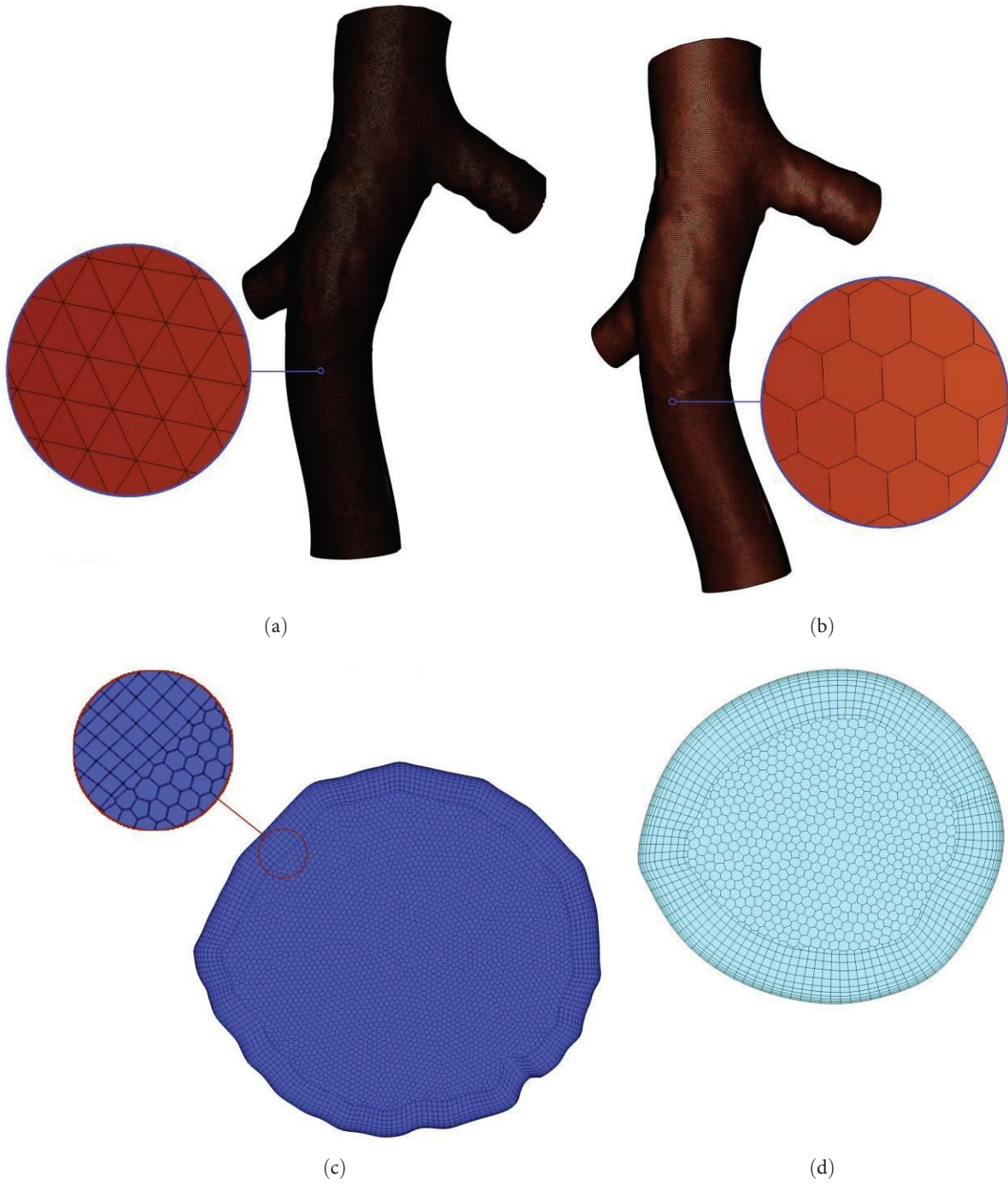


FIGURE 4: (a) Mesh with tetrahedral cells; (b) mesh with polyhedral cells (used in this study); (c and d) details of selected mesh in outlet and inlet areas, respectively.

define these cyclic variations. OSI is a helpful measure for calculating the average time of flow separation and reattachment [56]. Greater OSI values indicate areas where flow direction changes more frequently, while a lack of WSS cyclic variations is associated with smaller OSI values [57]. OSI value ranges from zero (pure unidirectional flows) to 0.5 (totally oscillatory flows) [58]. For pure pulsatile flows, OSI is calculated as follows [30, 59]:

$$\text{OSI} = \frac{1}{2} \left(1 - \frac{\left| \frac{1}{T} \int_0^T \tau_s \, dt \right|}{\frac{1}{T} \int_0^T |\tau_s| \, dt} \right). \quad (9)$$

RRT variable assesses the distribution of frictional forces on the inside surface of the vessel. The RRT is shown to be a

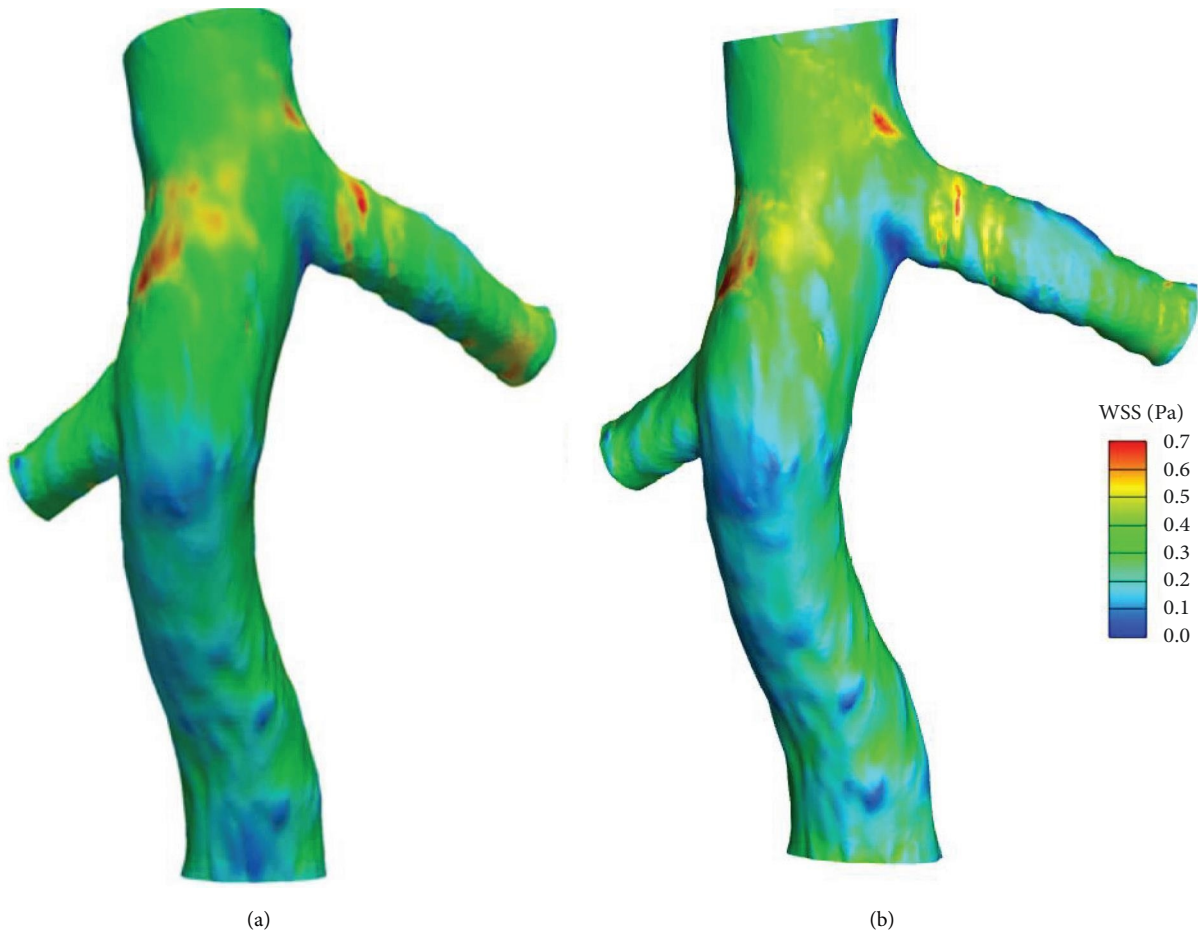


FIGURE 5: (a) WSS distribution predicted by López et al. [44]; (b) WSS distribution predicted by the present model.

vessel surface that is simultaneously subjected to low and oscillating WSSs [60]. RRT is a measure of how close the particles remain to the wall and is calculated as follows [30, 59]:

$$\text{RRT} = \frac{1}{(1 - 2\text{OSI}) \cdot \text{TAWSS}}. \quad (10)$$

3. Results

3.1. Time-Averaged Wall Shear Stress (TAWSS). TAWSS contours for different modes are shown in Figure 6. Figure 7 also shows contours for each simulation based on the difference in shear stress values compared to the case without a filter ($\text{TAWSS} - \text{TAWSS}_{\text{without filter}}$). These contours make it easier to assess the effect of the filter and clot on hemodynamic parameters. As shown in all figures, there is an area with less shear stress before the renal veins, while after the right renal vein, TAWSS increases due to an increase in the flow rate and, consequently, the average velocity in the vein. Shear stress increases again after blood flow in the left renal vein adds to the IVC blood flow.

Because of filter implantation, there is not much general change in the magnitude of TAWSS. This result is consistent

with prior studies [3]. The only obvious consequence of the implantation of the filter appears in areas with very low shear stresses around the filter.

Trapping a small clot in the filter has minimal effect on the TAWSS values on the IVC wall. However, TAWSS increases slightly downstream of the filter (Figure 7). In the region before the conjunction of the right renal vein, which has the lowest values of WSS, TAWSS slightly reduces due to the presence of a small clot. As the clot size increases to medium size, TAWSS increases downstream of the filter, and its reduction before the conjunction of the right renal vein is more visible. These changes reach their maximum values with increasing clot size to a large clot.

Figure 8 shows the average TAWSS changes along the vein as a percentage compared to the IVC without filter case. The effect of the filter and captured clot increases by enlarging the clot size. In the case of the filter with a large clot, the average TAWSS change sharply rises at the clot location (just under 300%). A slight decrease in the value of average TAWSS change is seen after the clot (about 10%).

Figure 9 shows TAWSS distribution on the surface of the captured clots for three different clot sizes. There is an area with high TAWSS on the small clot. As the size of the clot increases, the value of the maximum TAWSS on the clot decreases. The most important area in these figures is on

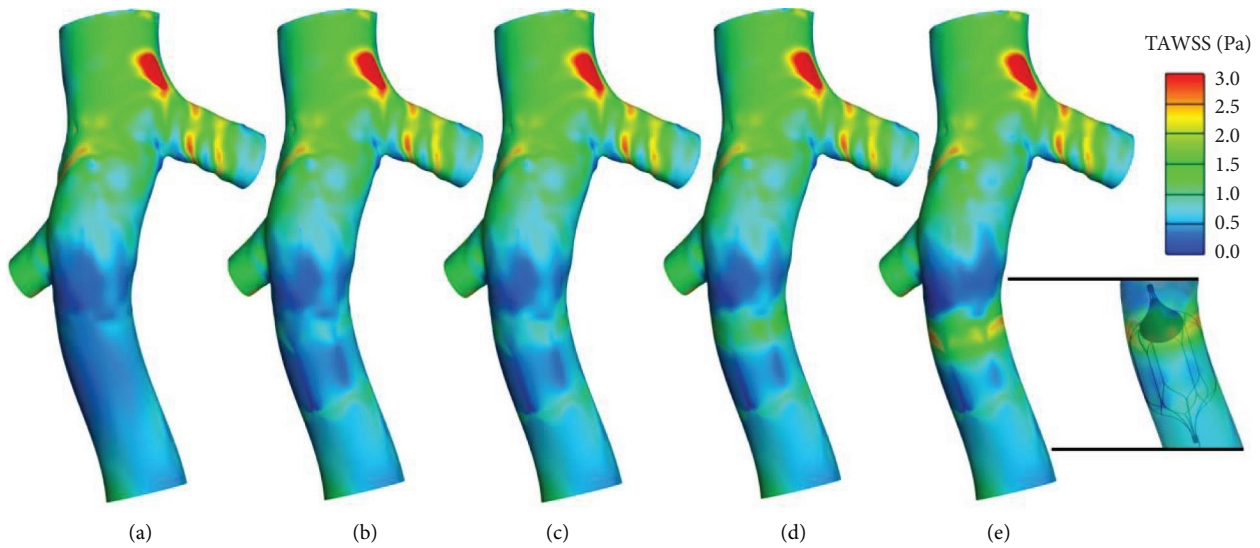


FIGURE 6: TAWSS contours on the IVC wall for different cases: (a) IVC without a filter; (b) IVC with an unoccluded filter; (c) IVC with a filter and a small captured clot; (d) IVC with a filter and a medium captured clot; (e) IVC with a filter and a large captured clot.

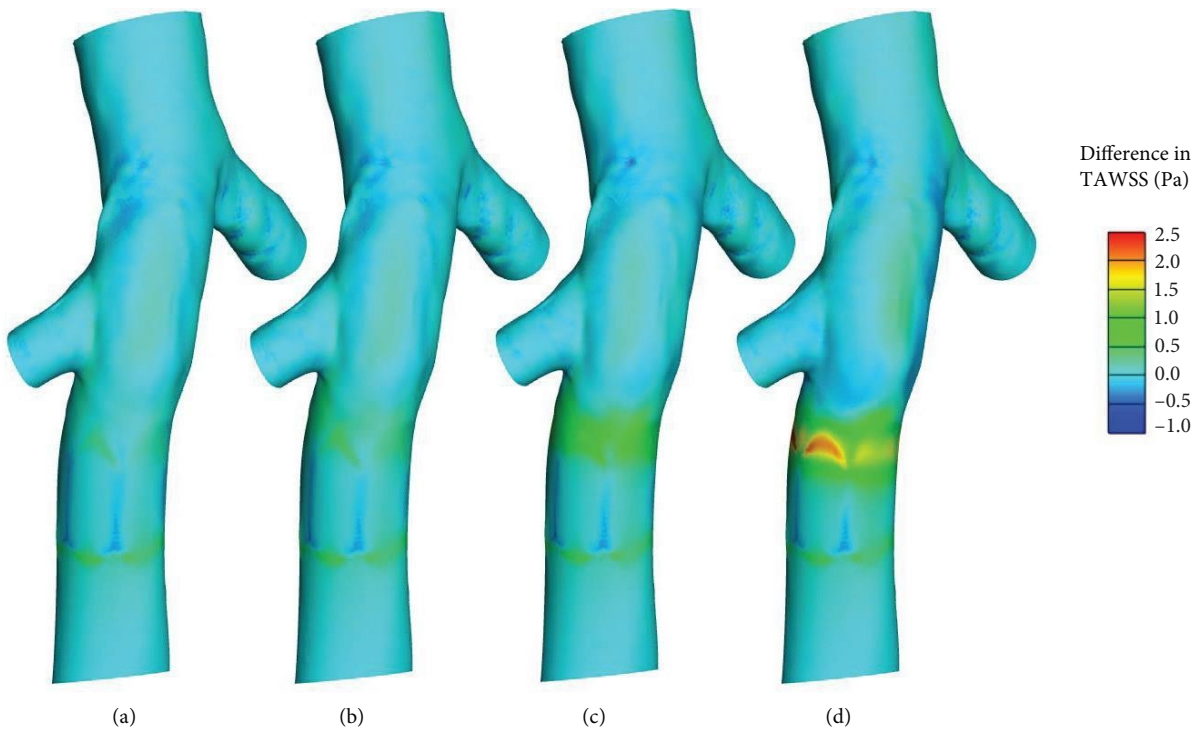


FIGURE 7: Difference in TAWSS contours on the IVC wall for different cases compared to the case without filter: (a) IVC with an unoccluded filter; (b) IVC with a filter and a small captured clot; (c) IVC with a filter and a medium captured clot; (d) IVC with a filter and a large captured clot.

the opposite side of the clot, with a relatively large area with low TAWSS.

3.2. Oscillating Shear Index (OSI). Figure 10 shows OSI contours for five different conditions. Without filter implantation, the highest OSI value is associated with the junction of the renal veins with the IVC. The OSI difference contours are shown in Figure 11 to help understand the filter and clot

effect on OSI distribution. These contours show the difference in OSI values between the cases, including the filter and the case without the filter ($OSI - OSI_{\text{without filter}}$). After the implantation of filters, very small regions with higher OSI appear on the IVC wall close to the filter. Capturing a small clot in the filter does not make a meaningful difference in OSI distribution compared to the unoccluded filter case. However, by increasing the size to a medium clot, an area

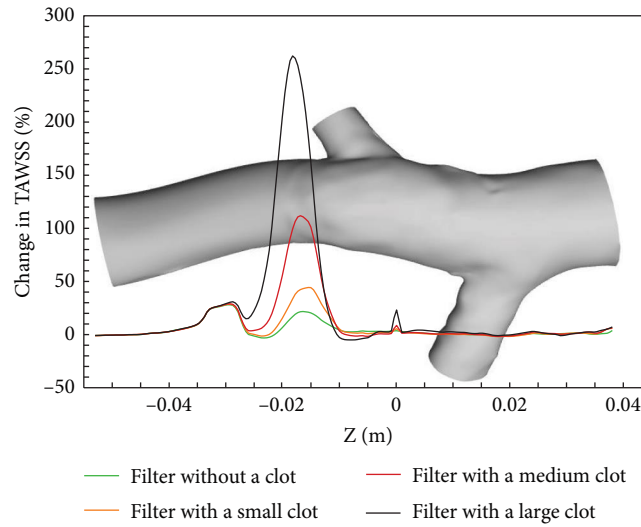


FIGURE 8: Average percentage change in TAWSS along the Z direction in comparison to the case without a filter.

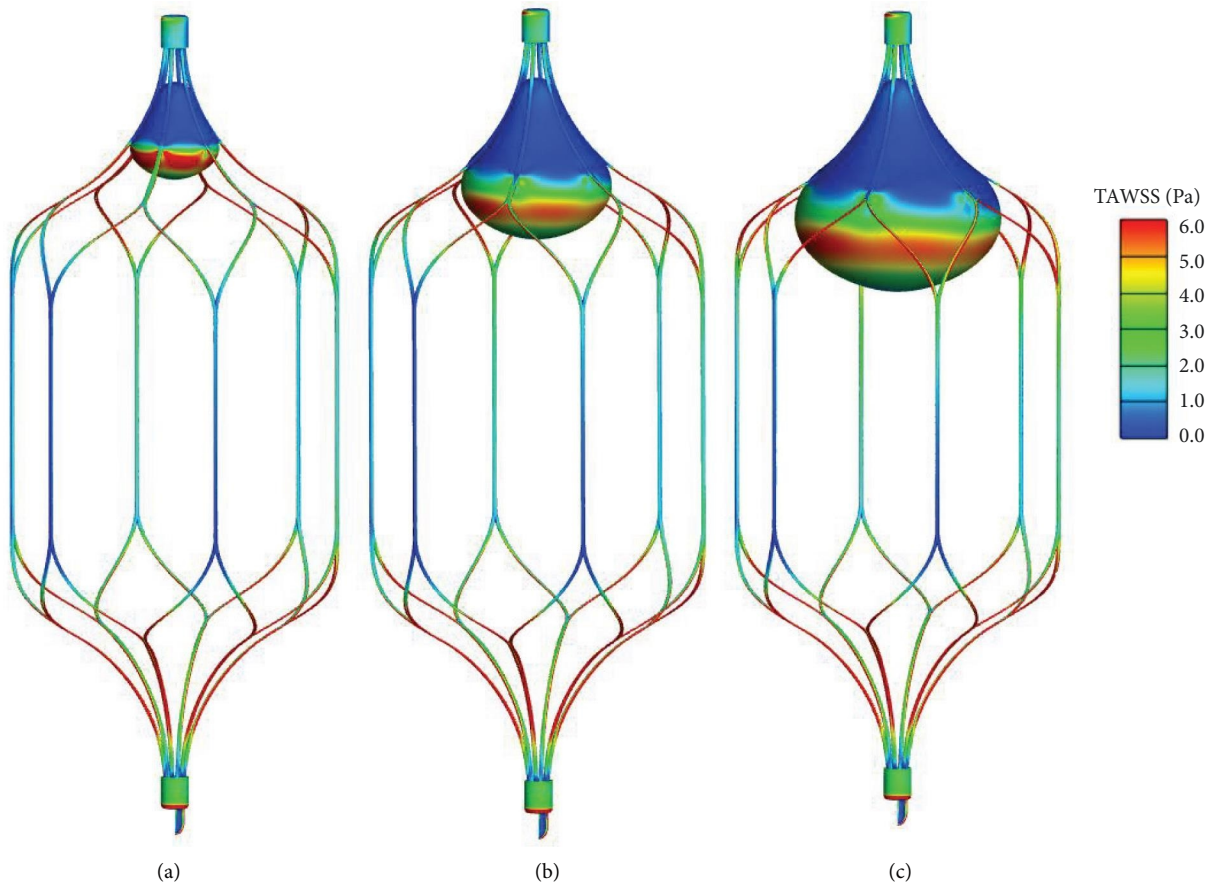


FIGURE 9: TAWSS contours on the clot surface for different cases: (a) IVC with a filter and a small captured clot; (b) IVC with a filter and a medium captured clot; (c) IVC with a filter and a large captured clot.

with moderate OSI values appears after the conjunction of the right renal vein and before the left renal vein. The magnitude of the OSI in this area rises more with increasing clot size from medium to large clot.

In addition, the magnitude of the OSI in the area around the conjunction of the left renal vein increases slightly by increasing the size of the clot from small to medium, which is due to the effect of the clot on the flow turbulence in this

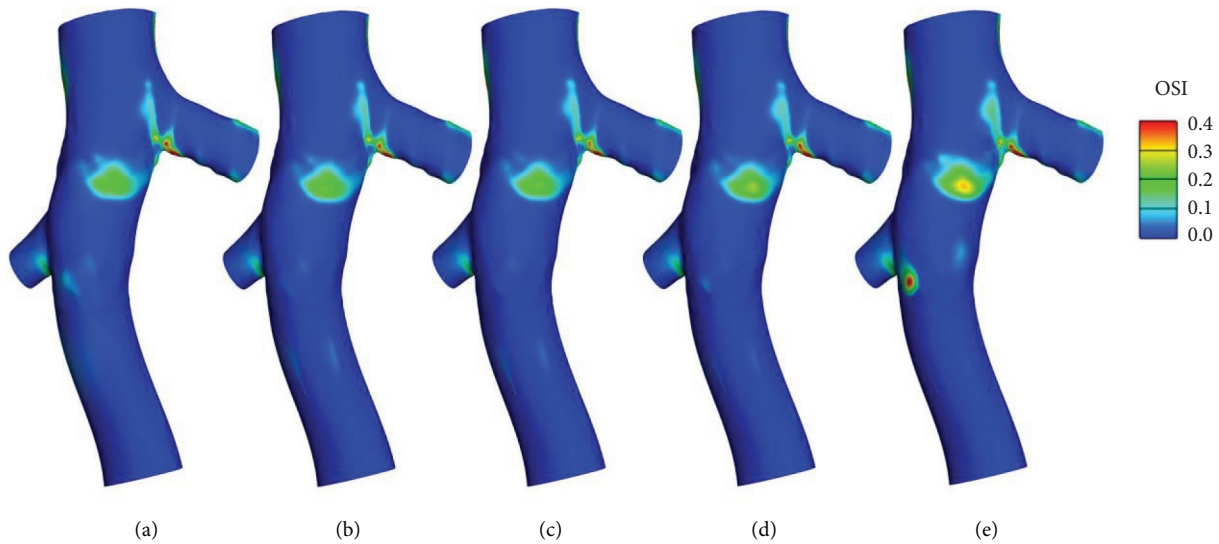


FIGURE 10: OSI contours on the IVC wall for different cases: (a) IVC without a filter; (b) IVC with an unoccluded filter; (c) IVC with a filter and a small captured clot; (d) IVC with a filter and a medium captured clot; (e) IVC with a filter and a large captured clot.

area. The values of OSI in this area increase more in case of capturing a large clot.

The region that garners the most attention in the OSI distribution is located after the clot in the large clot case. In this area which had an extremely low TAWSS value (Figures 6 and 7), the OSI parameter is significantly high.

Figure 12 shows the average changes in OSI value along the Z direction for various cases compared to the IVC without filter case. It was impossible to present these changes in percent because the OSI value in a large area of the vein wall was zero. The average OSI at the clot location decreases according to the graphs. Certainly, the effect is more significant for larger clots. After the clot, the average OSI value rises, especially in cases, including larger clots.

Figure 13 shows the OSI contours on the surface of three different clot sizes. On the anterior surface of the clot, it shows a large area with high OSI. From the OSI comparisons on the clot, it is clear that as the clot size increases, the OSI magnitude goes up.

3.3. Relative Residence Time (RRT). Figure 14 shows the RRT contours for different conditions. The difference in RRT values for each case compared to the empty vein case ($RRT - RRT_{\text{without filter}}$) has also been shown in Figure 15 in order to more thoroughly investigate the impact of adding a filter and clot to the vein. Considering the first case, in which there is no filter, it can be observed that the only place with a high RRT value is the conjunction of the left renal vein with IVC. After implantation of the filter, it is observed that places with relatively high RRT appear around the filter.

The effect of a small clot on the RRT contour is not significant. But with increasing clot size to medium, an area with moderate RRT appears after the filter. As shown in Figure 14(e) and Figure 15(d), the effect of a large clot on the RRT magnitude in this area is undeniable.

As shown in Figure 16, the average changes in the RRT parameter compared to the case of the vein without filter case

along the Z direction have been presented in percent. Due to the increase of the TAWSS and decrease of the OSI at the location of the clot, the RRT's average value decreases significantly (about 70%). In the presence of a filter with a large clot, the average RRT increases about 15% after the clot location.

The RRT parameter is more effective than other parameters in finding the regions prone to thrombogenesis. Hence, as shown in Figure 17, RRT contours are presented on the clot. There are vast areas in the anterior surface of the clots with high RRT values.

4. Discussion

4.1. TAWSS. For determining the rate of progression of cardiovascular diseases like atherosclerosis and thrombosis, a reduction in the value of TAWSS on the vessel wall is generally the most important factor [61, 62]. Clinical evidence shows that TAWSS, in addition to affecting the initial formation of plaque and thrombus, also plays an important role in their development [63]. Although low shear stress has always been cited as a cause of vascular occlusion diseases [64, 65], high shear stress can also cause these types of diseases [66, 67]. High shear stresses and turbulence cause damage to endothelial cells [68], play an important role in platelet activation, and may cause plaque rupture [69].

Due to empty filter implantation, some areas with low TAWSS around the filter have appeared. These areas can be ideal areas from a hemodynamical point of view for thrombosis and emboli growth, as also mentioned in prior studies [5]. As was observed, trapping a small clot in the filter leads to an increase in the TAWSS downstream of the filter, but it is not enough to damage endothelial cells or activate platelets. Platelet activation due to high shear stress, considered one of the primary mechanisms of thrombogenesis, is possible at values above 5 Pa [22, 70]. Due to their central location,

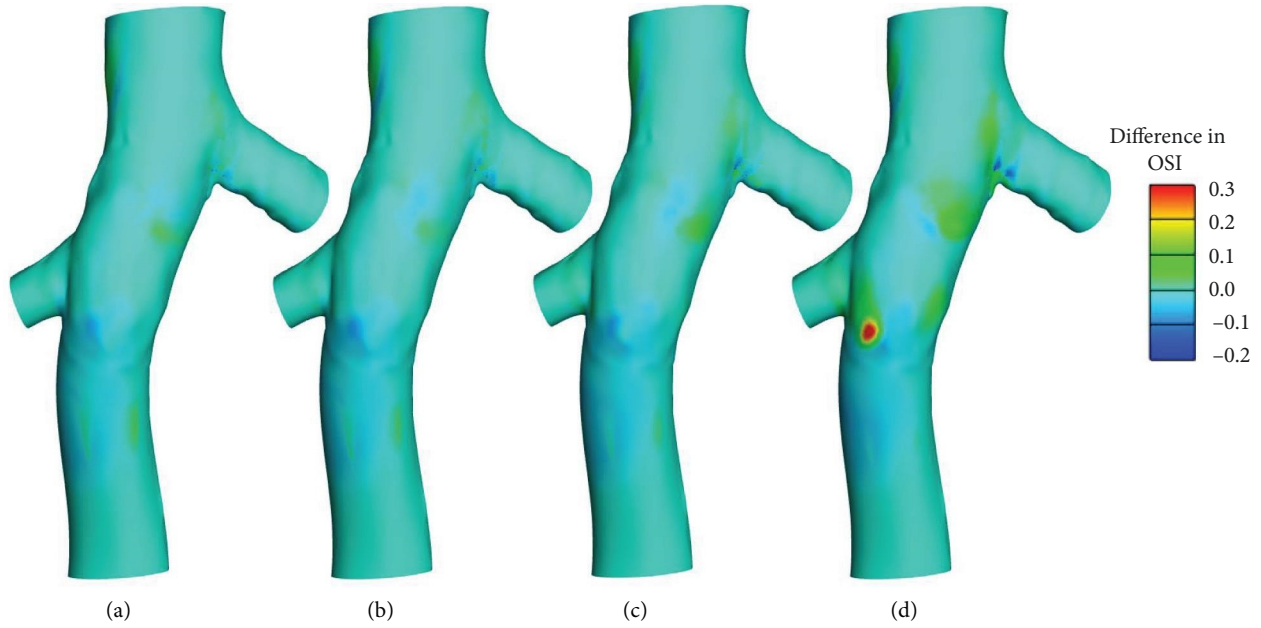


FIGURE 11: Difference in OSI contours on the IVC wall for different cases: (a) IVC with an unoccluded filter; (b) IVC with a filter and a small captured clot; (c) IVC with a filter and a medium captured clot; (d) IVC with a filter and a large captured clot.

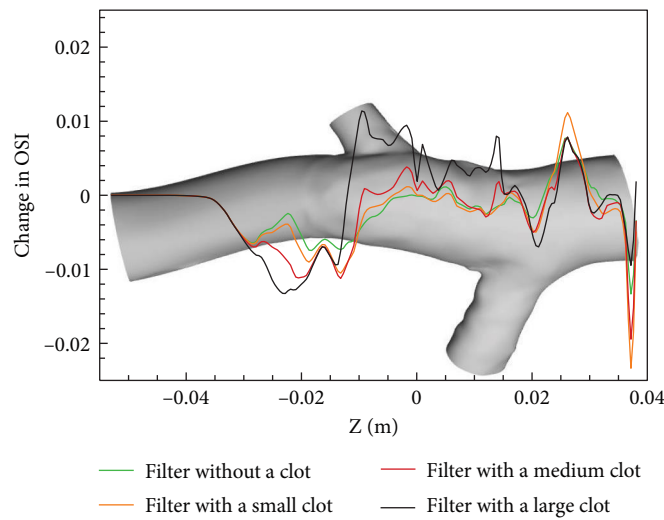


FIGURE 12: Average change in OSI along the Z direction in comparison to the case without a filter.

these clots guide blood flow to the wall. This phenomenon produces high-velocity gradients near the wall, resulting in high WSS values. This result is consistent with the results of previous studies [4]. If there is a larger clot in the filter, TAWSS before the right renal vein increases further and can create a dangerous thrombogenic region. A great rise in the value of average TAWSS (Figure 8) is another evidence of this claim. As was noted in the Results section, the decrease in TAWSS downstream of the filter becomes more obvious as the clot size increases. As a result, this region can be labeled as a prone region for the formation of the initial plaques.

Figure 9 shows some areas with high TAWSS on clots. In the absence of endothelial cells, there is no threat from this

area. A more important area is on the other side of the clot, where there is a sizable area with low TAWSS. As was stated, these regions are prone to thrombus growth. In addition, this region gets wider as the clot grows larger.

4.2. *OSI*. Regions of the vessel wall exposed to highly fluctuating WSS values during the cardiac cycle are identified using OSI [71]. These areas frequently include rotational flows and vortex production, which are closely related to atherosclerotic plaque development [72]. It has been demonstrated that OSI is an appropriate criterion in oscillating blood flow, although the process of thrombus development depends on several biological aspects [9, 73]. According to the experimental results, the thrombus formation locations have high

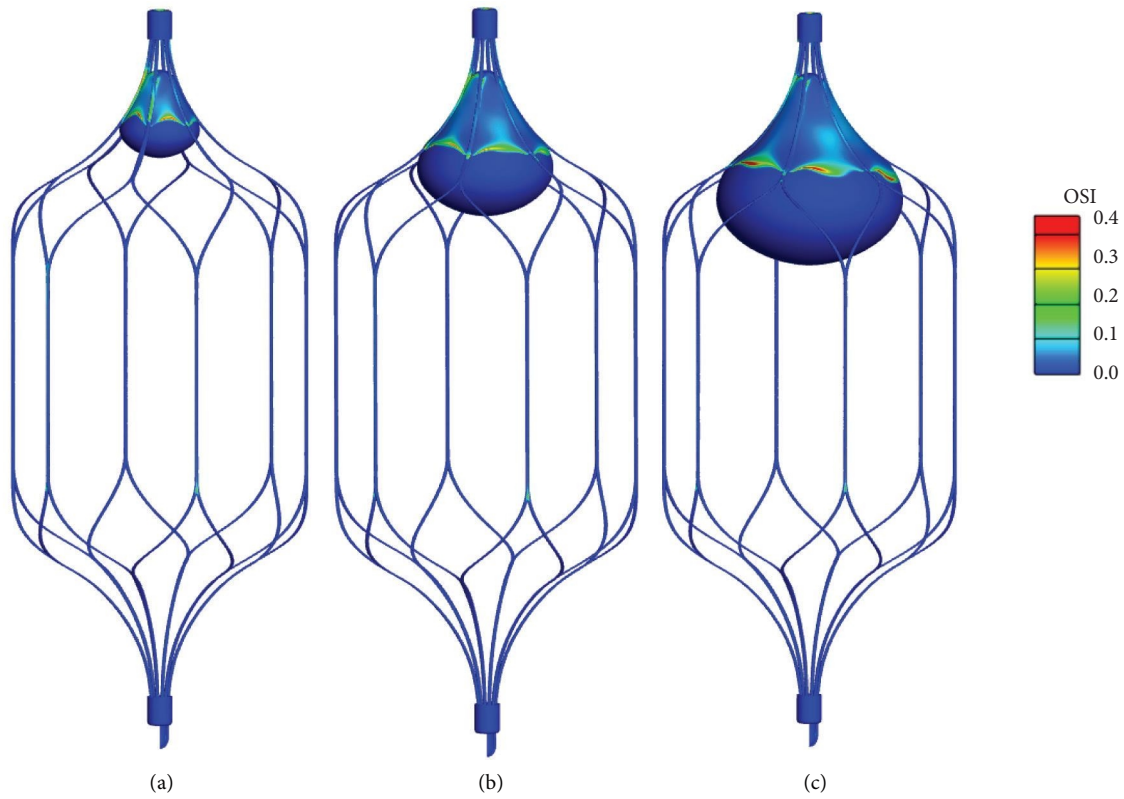


FIGURE 13: OSI contours on the filter and clot surface for different cases: (a) IVC filter and a small captured clot; (b) IVC filter and a medium captured clot; (c) IVC filter and a large captured clot.

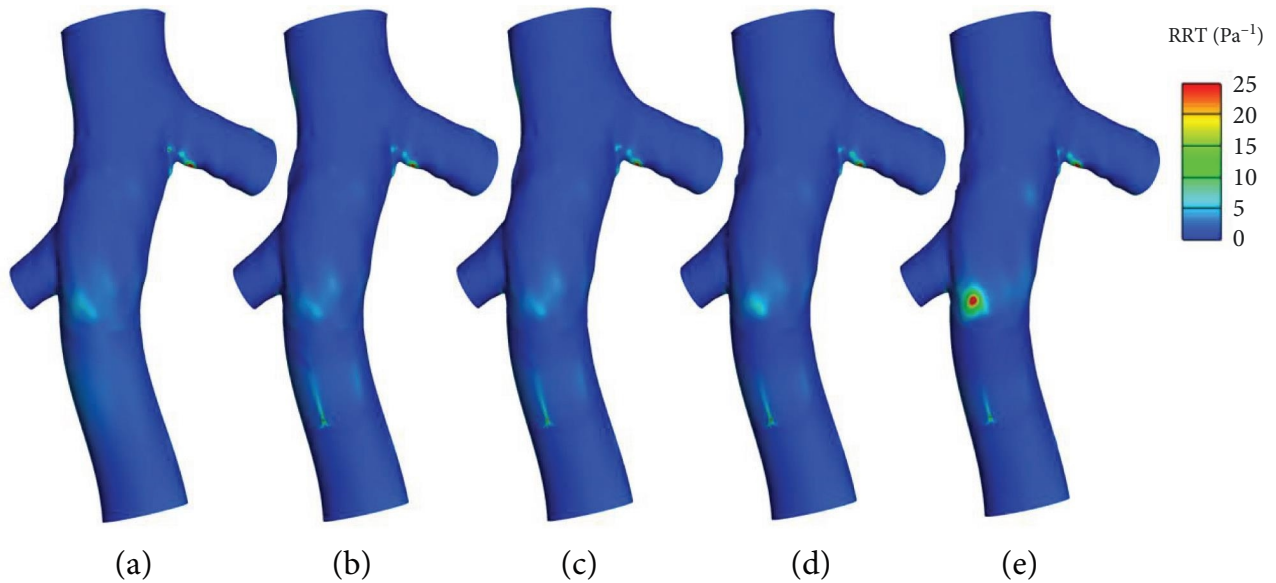


FIGURE 14: RRT contours on IVC wall for different cases: (a): IVC without a filter; (b) IVC with an unoccluded filter; (c) IVC with a filter and a small captured clot; (d) IVC with a filter and a medium captured clot; (e) IVC with a filter and a large captured clot.

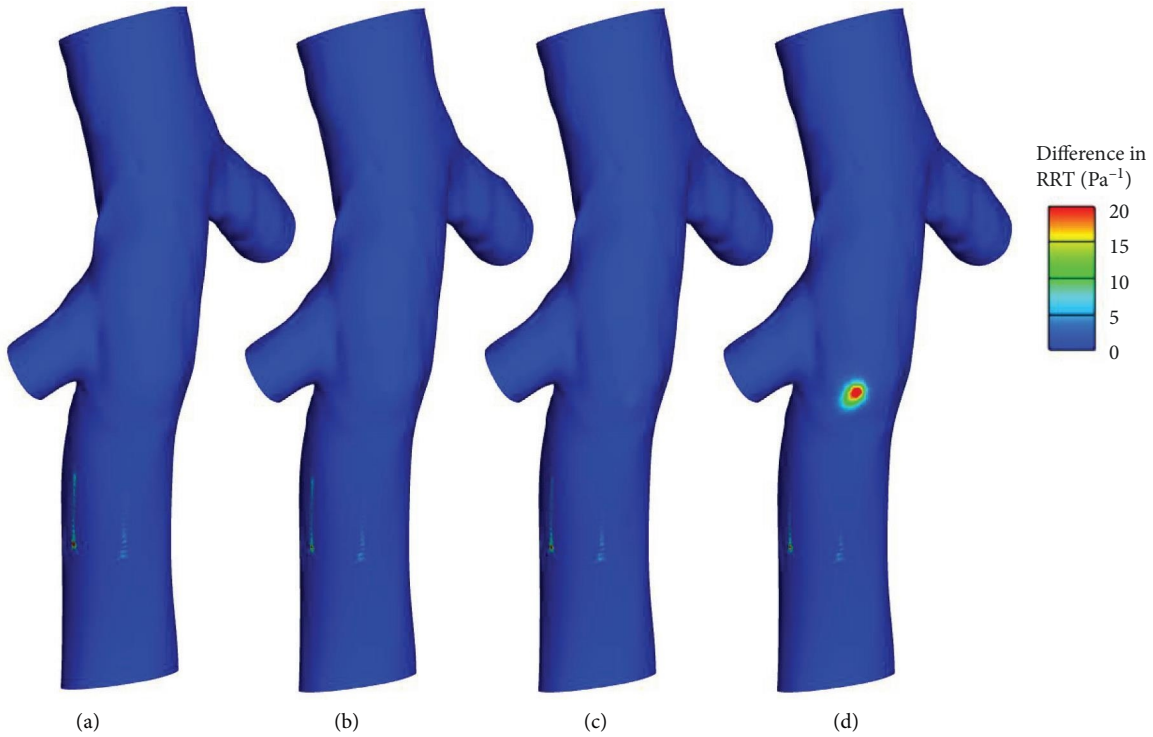


FIGURE 15: Difference in RRT contours on IVC wall for different cases: (a) IVC with an unoccluded filter; (b) IVC with a filter and a small captured clot; (c) IVC with a filter and a medium captured clot; (d) IVC with a filter and a large captured clot.

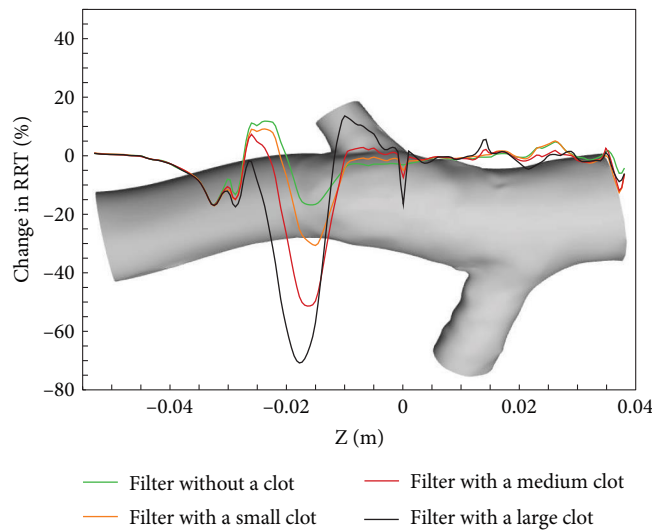


FIGURE 16: Average percentage change in RRT along Z direction in comparison to the case without a filter.

OSI values and low shear stress [74, 75]. The risk of occlusion is related to the local WSS and OSI close to the vessel wall [76]. However, compared to clinical data, the OSI factor predicts the disease risk better [77]. Studies show that severe oscillating WSS causes fatigue lesions of the intima vascular layer, atherosclerosis, and blockages [61].

The highest OSI values in the empty vein case occur at the conjunction of the renal veins and the IVC. In addition to the geometry curvatures, the reason for this is due to the mixing of the blood flowing out of the renal veins with the

blood flow in the IVC. Implantation of filters makes small regions appear with higher OSI around the filter, although the average OSI value in this area decreases. Due to the low values of TAWSS in these areas, it can be concluded that the filter without captured clot creates an area with low TAWSS and high OSI around it, which causes the accumulation of particles and help to form plaques in these regions. As it was compared to the unoccluded filter case, capturing a small clot in the filter makes no meaningful difference in OSI distribution. The value of OSI in a region after the conjunction of the

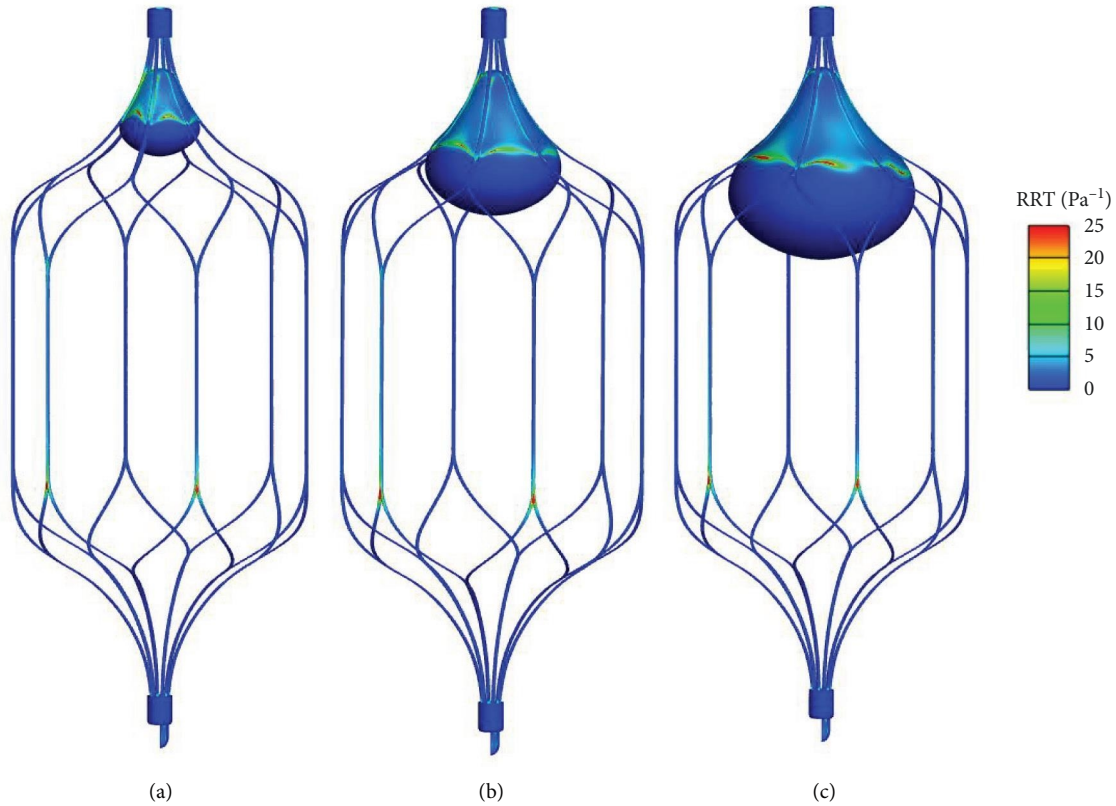


FIGURE 17: RRT contours on filter and clot surface for different cases: (a) IVC filter and a small captured clot; (b) IVC with a filter and a medium captured clot; (c) IVC with a filter and a large captured clot.

right renal vein and before the left renal vein rises by increasing the clot size. Since the values of TAWSS in this region are not very low, it is not possible to give a definite statement about the susceptibility of this area to caval occlusion or thrombosis. In addition, by increasing the clot size, the OSI value in the area around the conjunction of the left renal vein increases. Due to the low TAWSS in this area, this area can be mentioned as a suitable place for the accumulation and formation of particles and the growth of thrombus. As shown in Figures 11 and 12, an area with high OSI and low TAWSS has appeared after the filter because of capturing a large clot. Low TAWSS and high OSI are the main features of areas with stagnant flow and recirculation flow that have been mentioned as suitable environments for thrombus growth [5]. Therefore, this place can be identified as one of the most prone places to the formation and growth of plaque and thrombus.

Due to the sudden expansion of the flow cross-sectional area and, consequently, a high positive pressure gradient, a region with high OSI on the anterior clot surface was expected. The magnitude of OSI and the area of this region increases as the clot size grows. In previous studies, it has been stated that as a general trend, the size of the recirculation area increases with blood flow velocity and clot volume [4]. Due to the low TAWSS values in these areas, the possibility of IVC thrombosis increases as the clot becomes larger. This leads to increasing the volume of the clot with time.

4.3. *RRT*. The residency period of particles along the wall is proportional to the combination of OSI and TAWSS, and this index has a clear relation with the biological mechanisms of thrombosis [78]. Elevated OSI levels are often associated with low TAWSS and together act as indicators of vascular injury [79]. But areas with high OSI values do not necessarily correspond to areas with low TAWSS values [80]. In hemodynamic studies, RRT is used as a robust metric to identify areas with low WSS and high oscillation [60].

Based on RRT contours, before implantation of the filter, the only place prone to primary plaque formation and thrombus is the conjunction of the left renal vein with IVC. Implantation of the filter leads to appearing some places with high RRT around the filter. RRT contours, similar to OSI and TAWSS contours, prove that these areas are at high risk for the accumulation of particles and the formation of plaques. Like in the TAWSS and OSI analysis, a small clot has no meaningful effects. However, by increasing the clot size, an area with higher RRT values appears after the clot. This place should be marked as an area prone to primary plaque formation and exacerbation of IVC thrombosis.

As shown in Figure 16, we can see that the value of RRT at the location of the clot is significantly reduced in the case of a large clot. Since the RRT value in the IVC without filter case is very low in this location, this decrease in the RRT value is not important. As mentioned in TAWSS analysis, the only important thing in this region is a significant increase in

TAWSS due to the presence of the filter with a large clot, which may damage endothelial cells or platelet activation.

As was mentioned in the simultaneous analysis of TAWSS and OSI, the anterior surface of the clot is highly susceptible to thrombus growth. The maximum value of RRT and OSI occurs where the probability of starting flow separation is high. Due to wide areas in the anterior surface of the clot, these locations are thought to be the best places for thrombus growth. As a result, the volume of clots increases with time, increasing the risk of plaque formation and thrombus growth on the IVC wall.

5. Conclusion

Using a filter for patients with PE can be helpful alongside anticoagulants. However, the effectiveness of these filters has always been debated. According to studies, so far, no numerical study has been performed to simulate the IVC with a filter using physiological pulses. In this study, for the first time, hemodynamic parameters were used to simulate blood flow in an IVC in different conditions. The results indicated a low effect of an unoccluded filter. The IVC regions close to the filter can be identified as places with a high possibility of particle accumulation. Trapping a small clot also has a small effect on TAWSS. The effect of adding a small clot on OSI and RRT parameters is negligible. As the clot size increases, areas with very low shear stress and high OSI emerge, which can be described as thrombogenic areas and exacerbate IVC thrombosis. The exact location of these areas was determined by RRT analysis. This parameter predicts the area after the filter and also the area around the filter as areas with the highest possibility of plaque formation and thrombus growth. In addition, when large clots are trapped in the filter, the value of TAWSS increases, and there is the risk of damage to endothelial cells and platelet activation. It has also been shown that the anterior surface of the clot is an ideal place for thrombus growth due to its low TAWSS and high OSI and RRT. Consequently, the volume of the clot increases with time, and, as a result, the risk of plaque formation and thrombus growth on the IVC wall increases.

Nomenclature

3D:	Three-dimensional
α^* :	Low Reynolds number corrector
$\dot{\gamma}$:	Shear rate
M :	Dynamic viscosity
μ_0 :	Viscosity at zero shear rate
μ_∞ :	Viscosity at infinite shear rate
μ_t :	Dynamic turbulent viscosity
ρ :	Density
σ_ω :	2.0, Turbulent Prandtl numbers for ω
σ_k :	1.0, Turbulent Prandtl numbers for k
T :	Shear stress
Ω :	Specific dissipation rate
CFD:	Computational fluid dynamics
DVT:	Deep vein thrombosis
F:	External body forces
G_ω :	Generation of ω

G_k :	Generation of turbulence kinetic energy due to mean velocity gradients
IVC:	Inferior vena cava
MUSCL:	Monotonic upstream-centered scheme for conservation laws
OSI:	Oscillating shear index
PE:	Pulmonary embolism
RRT:	Relative residence time
S:	Modulus of the mean strain rate tensor
S_k, S_ω :	User-defined source terms
TAWSS:	Time-averaged wall shear stress
WSS:	Wall shear stress
Y_ω :	Dissipation of ω due to turbulence
Y_k :	Dissipation of k due to turbulence
K:	Turbulence kinetic energy
$k-\omega$:	Standard $k-\omega$ model
p:	Pressure
u:	Velocity of fluid flow.

Data Availability

The data used to support the findings of this study are available from the corresponding author upon request.

Additional Points

Limitations. We had some limitations in this study, just like any other study. One of our study's limitations was the impossibility of measuring the patient-specific boundary condition. Therefore, the boundary conditions from earlier studies were used. The lack of clinical data validation was another limitation. The solution model was initially validated with one of the earlier studies in this field because there were no clinical data on this subject. Lack of consideration for the IVC wall's elasticity is another limitation. The effects of the IVC filter with an elastic vein wall have not yet been studied, but we plan to conduct this research using a hyperelastic model in our future study.

Conflicts of Interest

The authors declare that they have no conflicts of interest.

Authors' Contributions

Conception and design: Jafar Moradicheghamahi; methodology: Jafar Moradicheghamahi, Muhammad Qasim, and Hamed Farokhi; numerical simulations: Jafar Moradicheghamahi and Muhammad Qasim; analysis and interpretation of data: Jafar Moradicheghamahi, Muhammad Qasim, and Sohrab Jafarpour; study supervision: Jafar Moradicheghamahi; writing original draft: Jafar Moradicheghamahi; writing review and editing: Jafar Moradicheghamahi and Hamed Farokhi. All authors have read and approved the final manuscript.

Acknowledgments

We would like to thank the Smart Technology for Smart Healthcare group of the University of Rovira and Virgili,

Prof. Josep M. Lopez, Prof. Gerard Fortuny, Prof. Juan Herrero, and Prof. Dolores Puigjaner for sharing the geometry with us. Open access funding was enabled and organized by CRUE-CSUC Gold.

References

- [1] S. Z. Goldhaber and H. Bounameaux, "Pulmonary embolism and deep vein thrombosis," *The Lancet*, vol. 379, no. 9828, pp. 1835–1846, 2012.
- [2] N. Mackman, "Triggers, targets and treatments for thrombosis," *Nature*, vol. 451, no. 7181, pp. 914–918, 2008.
- [3] K. I. Aycock, R. L. Campbell, K. B. Manning et al., "A computational method for predicting inferior vena cava filter performance on a patient-specific basis," *Journal of Biomechanical Engineering*, vol. 136, no. 8, 2014.
- [4] J. M. López, G. Fortuny, D. Puigjaner, J. Herrero, and F. Marimon, "Hemodynamic effects of blood clots trapped by an inferior vena cava filter," *International Journal for Numerical Methods in Biomedical Engineering*, vol. 36, no. 7, p. e3343, 2020.
- [5] A. Harlal, M. Ojha, and K. W. Johnston, "Vena cava filter performance based on hemodynamics and reported thrombosis and pulmonary embolism patterns," *Journal of Vascular and Interventional Radiology*, vol. 18, no. 1, pp. 103–115, 2007.
- [6] F. Zhang, D. Li, J. Liu, and H. Zhang, "The vena tech LP permanent caval filter: effectiveness and safety in the clinical setting in three chinese medical centers," *Thrombosis Research*, vol. 136, no. 1, pp. 40–44, 2015.
- [7] H. Decousus, A. Leizorovicz, F. Parent et al., "A clinical trial of vena caval filters in the prevention of pulmonary embolism in patients with proximal deep-vein thrombosis," *New England Journal of Medicine*, vol. 338, no. 7, pp. 409–416, 1998.
- [8] R. Kalbasi, B. Sharifzadeh, and M. Jahangiri, "Investigation of artery wall elasticity effect on the prediction of atherosclerosis by hemodynamic factors," *Applied Bionics and Biomechanics*, vol. 2022, Article ID 3446166, 17 pages, 2022.
- [9] J. Moradicheghamahi, J. Sadeghisaraji, and M. Jahangiri, "Numerical solution of the pulsatile, non-Newtonian and turbulent blood flow in a patient specific elastic carotid artery," *International Journal of Mechanical Sciences*, vol. 150, pp. 393–403, 2019.
- [10] R. L. Leask, K. W. Johnston, and M. Ojha, "In vitro hemodynamic evaluation of a Simon nitinol vena cava filter: possible explanation of IVC occlusion," *Journal of Vascular and Interventional Radiology*, vol. 12, no. 5, pp. 613–618, 2001.
- [11] G. G. Couch, K. W. Johnston, and M. Ojha, "An in vitro comparison of the hemodynamics of two inferior vena cava filters," *Journal of Vascular Surgery*, vol. 31, no. 3, pp. 539–549, 2000.
- [12] S. P. Sastry, J. Kim, S. M. Shontz et al., "Patient-specific model generation and simulation for pre-operative surgical guidance for pulmonary embolism treatment," in *Image-Based Geometric Modeling and Mesh Generation*, pp. 223–249, Springer, 2013.
- [13] T. Swaminathan, H. H. Hu, and A. A. Patel, "Numerical analysis of the hemodynamics and embolus capture of a Greenfield vena cava filter," *Journal of Biomechanical Engineering*, vol. 128, no. 3, pp. 360–370, 2006.
- [14] M. A. Singer, W. D. Henshaw, and S. L. Wang, "Computational modeling of blood flow in the TrapEase inferior vena cava filter," *Journal of Vascular and Interventional Radiology*, vol. 20, no. 6, pp. 799–805, 2009.
- [15] M. B. Streiff, "Vena caval filters: a comprehensive review," *Blood*, vol. 95, no. 12, pp. 3669–3677, 2000.
- [16] P. S. Group, "Eight-year follow-up of patients with permanent vena cava filters in the prevention of pulmonary embolism: the PREPIC (Prevention du Risque d'Embolie Pulmonaire par Interruption Cave) randomized study," *Circulation*, vol. 112, no. 3, pp. 416–422, 2005.
- [17] S. Wessler, "Thrombosis in the presence of vascular stasis," *The American Journal of Medicine*, vol. 33, no. 5, pp. 648–666, 1962.
- [18] S. F. Stewart, R. A. Robinson, R. A. Nelson, and R. A. Malinauskas, "Effects of thrombosed vena cava filters on blood flow: flow visualization and numerical modeling," *Annals of Biomedical Engineering*, vol. 36, no. 11, pp. 1764–1781, 2008.
- [19] R. L. Leask, K. W. Johnston, and M. Ojha, "Hemodynamic effects of clot entrapment in the TrapEase inferior vena cava filter," *Journal of Vascular and Interventional Radiology*, vol. 15, no. 5, pp. 485–490, 2004.
- [20] E. Rahbar, D. Mori, and J. E. Moore Jr, "Three-dimensional analysis of flow disturbances caused by clots in inferior vena cava filters," *Journal of Vascular and Interventional Radiology*, vol. 22, no. 6, pp. 835–842, 2011.
- [21] Z. Ren, S. L. Wang, and M. A. Singer, "Modeling hemodynamics in an unoccluded and partially occluded inferior vena cava under rest and exercise conditions," *Medical & Biological Engineering & Computing*, vol. 50, no. 3, pp. 277–287, 2012.
- [22] V. T. Turitto and C. L. Hall, "Mechanical factors affecting hemostasis and thrombosis," *Thrombosis Research*, vol. 92, no. 6, pp. S25–S31, 1998.
- [23] K. I. Aycock, R. L. Campbell, F. C. Lynch, K. B. Manning, and B. A. Craven, "The importance of hemorheology and patient anatomy on the hemodynamics in the inferior vena cava," *Annals of Biomedical Engineering*, vol. 44, no. 12, pp. 3568–3582, 2016.
- [24] M. B. Gallagher, K. I. Aycock, B. A. Craven, and K. B. Manning, "Steady flow in a patient-averaged inferior vena cava—Part I: particle image velocimetry measurements at rest and exercise conditions," *Cardiovascular Engineering and Technology*, vol. 9, no. 4, pp. 641–653, 2018.
- [25] B. A. Craven, K. I. Aycock, and K. B. Manning, "Steady flow in a patient-averaged inferior vena cava—Part II: computational fluid dynamics verification and validation," *Cardiovascular Engineering and Technology*, vol. 9, no. 4, pp. 654–673, 2018.
- [26] M. Kim, T. Min, O.-K. Kwon et al., "Numerical study on proximal ischemia," *Journal of Mechanical Science and Technology*, vol. 29, no. 12, pp. 5523–5529, 2015.
- [27] K. Kanokjaruvijit, T. Donprai-On, N. Phanthura, P. Noidet, and J. Siripokharattana, "Wall shear stress and velocity distributions in different types of stenotic bifurcations," *Journal of Mechanical Science and Technology*, vol. 31, no. 5, pp. 2339–2349, 2017.
- [28] C. Kumawat, B. K. Sharma, and K. S. Mekheimer, "Mathematical analysis of two-phase blood flow through a stenosed curved artery with hematocrit and temperature dependent viscosity," *Physica Scripta*, vol. 96, no. 12, Article ID 125277, 2021.
- [29] A. M. Awad, K. S. Mekheimer, S. A. Elkilany, and A. Z. Zaher, "Leveraging elasticity of blood stenosis to detect the role of a non-Newtonian flow midst an arterial tube:

- Mazumdar and Keller models,” *Chinese Journal of Physics*, vol. 77, pp. 2520–2540, 2022.
- [30] J. Moradicheghamahi, M. Jahangiri, M. Mousaviraad, and M. R. Sadeghi, “Computational studies of comparative and cumulative effects of turbulence, fluid–structure interactions, and uniform magnetic fields on pulsatile non-Newtonian flow in a patient-specific carotid artery,” *Journal of the Brazilian Society of Mechanical Sciences and Engineering*, vol. 42, no. 10, pp. 1–22, 2020.
- [31] A. Chen, A. A. B. Basri, N. B. Ismail, M. Tamagawa, D. Zhu, and K. A. Ahmad, “Simulation of mechanical heart valve dysfunction and the non-Newtonian blood model approach,” *Applied Bionics and Biomechanics*, vol. 2022, Article ID 9612296, 14 pages, 2022.
- [32] T. Elnaqeeb, K. S. Mekheimer, and F. Alghamdi, “Cu-blood flow model through a catheterized mild stenotic artery with a thrombosis,” *Mathematical Biosciences*, vol. 282, pp. 135–146, 2016.
- [33] D. Bluestein, “Research approaches for studying flow-induced thromboembolic complications in blood recirculating devices,” *Expert Review of Medical Devices*, vol. 1, no. 1, pp. 65–80, 2014.
- [34] C. M. Prado, S. G. Ramos, J. Elias Jr, and M. A. Rossi, “Turbulent blood flow plays an essential localizing role in the development of atherosclerotic lesions in experimentally induced hypercholesterolaemia in rats,” *International Journal of Experimental Pathology*, vol. 89, no. 1, pp. 72–80, 2008.
- [35] M. Jahangiri, M. Saghafian, and M. R. Sadeghi, “Numerical study of turbulent pulsatile blood flow through stenosed artery using fluid-solid interaction,” *Computational and Mathematical Methods in Medicine*, vol. 2015, Article ID 515613, 10 pages, 2015.
- [36] P. D. Stein and H. N. Sabbah, “Measured turbulence and its effect on thrombus formation,” *Circulation Research*, vol. 35, no. 4, pp. 608–614, 1974.
- [37] Y. Xue, P. Gao, Y. Lin, and C. Dai, “Preliminary study of hemodynamics in human carotid bifurcation by computational fluid dynamics combined with magnetic resonance angiography,” *Acta Radiologica*, vol. 48, no. 7, pp. 788–797, 2007.
- [38] S. Bhushan, D. K. Walters, and G. W. Burgreen, “Laminar, turbulent, and transitional simulations in benchmark cases with cardiovascular device features,” *Cardiovascular Engineering and Technology*, vol. 4, no. 4, pp. 408–426, 2013.
- [39] M. R. Borse, *Turbulent Simulations of Feline Aortic Flow under Hypertrophic Cardiomyopathy Heart Condition*, Mississippi State University, 2016.
- [40] A. Fluent, *16.2: Fluent Theory Guide*, ANSYS Help Viewer.
- [41] J. Sadeghiseraji, J. Moradicheghamahi, and A. Sedaghatkish, “Investigation of a vortex tube using three different RANS-based turbulence models,” *Journal of Thermal Analysis and Calorimetry*, vol. 143, no. 6, pp. 4039–4056, 2021.
- [42] M. Jahangiri, M. Saghafian, and M. Sadeghi, “Effects of non-Newtonian behavior of blood on wall shear stress in an elastic vessel with simple and consecutive stenosis,” *Biomedical and Pharmacology Journal*, vol. 8, no. 1, pp. 123–131, 2015.
- [43] D. Wang, F. Serracino-Inglott, and J. Feng, “Numerical simulations of patient-specific models with multiple plaques in human peripheral artery: a fluid-structure interaction analysis,” *Biomechanics and Modeling in Mechanobiology*, vol. 20, no. 1, pp. 255–265, 2021.
- [44] J. M. López, G. Fortuny, D. Puigjaner, J. Herrero, and F. Marimon, “A comparative CFD study of four inferior vena cava filters,” *International Journal for Numerical Methods in Biomedical Engineering*, vol. 34, no. 7, Article ID e2990, 2018.
- [45] C. P. Cheng, R. J. Herfkens, and C. A. Taylor, “Inferior vena caval hemodynamics quantified in vivo at rest and during cycling exercise using magnetic resonance imaging,” *American Journal of Physiology-Heart and Circulatory Physiology*, vol. 284, no. 4, pp. H1161–H1167, 2003.
- [46] L. O. Muller, *Mathematical modelling and simulation of the human circulation with emphasis on the venous system: application to the CCSVI condition*, PhD thesis, University of Trento.
- [47] K. I. Aycock, R. L. Campbell, K. B. Manning et al., “A computational method for predicting inferior vena cava filter performance on a patient-specific basis,” *Journal of Biomechanical Engineering*, vol. 136, no. 8, Article ID 081003, 2014.
- [48] I. Ansys, *ANSYS Fluent-Theory Guide-Release 2020R1*, ANSYS Inc, 2020.
- [49] J. Moradicheghamahi, G. Fortuny, J. M. López, D. Puigjaner, J. Herrero, and Y. Azeli, “The effect of thoracic dimensions on compression depth during cardiopulmonary resuscitation,” *International Journal for Numerical Methods in Biomedical Engineering*, vol. 39, no. 7, p. e3718, 2023.
- [50] J. Moradicheghamahi, G. Fortuny, J. M. López, J. Herrero, and D. Puigjaner, “Deformation of the myocardium during CPR,” arXiv preprint arXiv: 2205.15804, 2022.
- [51] M. Sosnowski, J. Krzywanski, K. Grabowska, and R. Gnatowska, “Polyhedral meshing in numerical analysis of conjugate heat transfer,” in *EPJ Web of Conferences*, EDP Sciences, 2018.
- [52] J. Moradi Cheqamahi, M. Nili-Ahmadabadi, S. Akbarzadeh, and M. Saghafian, “Numerical analysis of turbocharger’s bearing using dynamic mesh,” *Journal of Applied Fluid Mechanics*, vol. 9, no. 5, pp. 2545–2557, 2016.
- [53] K. Zore, B. Sasanapuri, G. Parkhi, and A. Varghese, “Ansys mosaic poly-hexcore mesh for high-lift aircraft configuration,” in *21st AeSI Annual CFD Symposium*, 2019.
- [54] M. Jahangiri, M. Saghafian, and M. Sadeghi, “Numerical study of hemodynamic parameters in pulsatile turbulent blood flow in flexible artery with stenosis,” in *The 22st Annual International Conference on Mechanical Engineering-ISME2014*, Shahid Chamran University, Ahvaz, Iran, 2014.
- [55] N. T. Philip, B. S. V. Patnaik, and B. J. Sudhir, “Hemodynamic simulation of abdominal aortic aneurysm on idealised models: Investigation of stress parameters during disease progression,” *Computer Methods and Programs in Biomedicine*, vol. 213, Article ID 106508, 2022.
- [56] M. Jahangiri, M. Saghafian, and M. R. Sadeghi, “Numerical simulation of non-Newtonian models effect on hemodynamic factors of pulsatile blood flow in elastic stenosed artery,” *Journal of Mechanical Science and Technology*, vol. 31, no. 2, pp. 1003–1013, 2017.
- [57] J. Urevc, I. Žun, M. Brumen, and B. Štok, “Modeling the effect of red blood cells deformability on blood flow conditions in human carotid artery bifurcation,” *Journal of Biomechanical Engineering*, vol. 139, no. 1, Article ID 011011, 2017.
- [58] H. Aryan, B. Beigzadeh, and M. Siavashi, “Euler-lagrange numerical simulation of improved magnetic drug delivery in a three-dimensional CT-based carotid artery bifurcation,” *Computer Methods and Programs in Biomedicine*, vol. 219, Article ID 106778, 2022.
- [59] M. Teymoori, M. R. Sadeghi, M. Rabbani, and M. Jahangiri, “Effect of extended lipid core on the hemodynamic parameters:

- a fluid–structure interaction approach,” *Applied Bionics and Biomechanics*, vol. 2022, Article ID 2047549, 14 pages, 2022.
- [60] S.-W. Lee, L. Antiga, and D. A. Steinman, “Correlations among indicators of disturbed flow at the normal carotid bifurcation,” *Journal of Biomechanical Engineering*, vol. 131, no. 6, Article ID 061013, 2009.
- [61] D. N. Ku, D. P. Giddens, C. K. Zarins, and S. Glagov, “Pulsatile flow and atherosclerosis in the human carotid bifurcation. Positive correlation between plaque location and low oscillating shear stress,” *Arteriosclerosis: An Official Journal of the American Heart Association, Inc*, vol. 5, no. 3, pp. 293–302, 1985.
- [62] C. K. Zarins, D. P. Giddens, B. K. Bharadvaj, V. S. Sottiurari, R. F. Mabon, and S. Glagov, “Carotid bifurcation atherosclerosis. Quantitative correlation of plaque localization with flow velocity profiles and wall shear stress,” *Circulation Research*, vol. 53, no. 4, pp. 502–514, 1983.
- [63] C. Caro, J. Fitz-Gerald, and R. Schroter, “Atheroma and arterial wall shear-observation, correlation and proposal of a shear dependent mass transfer mechanism for atherogenesis,” *Proceedings of the Royal Society of London. Series B. Biological Sciences*, vol. 177, no. 1046, pp. 109–159, 1971.
- [64] E. Cecchi, C. Giglioli, S. Valente et al., “Role of hemodynamic shear stress in cardiovascular disease,” *Atherosclerosis*, vol. 214, no. 2, pp. 249–256, 2011.
- [65] C. Kleinstreuer, S. Hyun, J. Buchanan, P. Longest, J. P. Archie Jr, and G. A. Truskey, “Hemodynamic parameters and early intimal thickening in branching blood vessels,” *Critical Reviews™ in Biomedical Engineering*, vol. 45, no. 1–6, pp. 319–382, 2017.
- [66] J. J. Wentzel, E. Janssen, J. Vos et al., “Extension of increased atherosclerotic wall thickness into high shear stress regions is associated with loss of compensatory remodeling,” *Circulation*, vol. 108, no. 1, pp. 17–23, 2003.
- [67] A. K. Joshi, R. L. Leask, J. G. Myers, M. Ojha, J. Butany, and C. R. Ethier, “Intimal thickness is not associated with wall shear stress patterns in the human right coronary artery,” *Arteriosclerosis, Thrombosis, and Vascular Biology*, vol. 24, no. 12, pp. 2408–2413, 2004.
- [68] P. F. Davies, A. Remuzzi, E. J. Gordon, C. F. Dewey Jr, and M. A. Gimbrone Jr, “Turbulent fluid shear stress induces vascular endothelial cell turnover in vitro,” *Proceedings of the National Academy of Sciences of The United States of America*, vol. 83, no. 7, pp. 2114–2117, 1986.
- [69] N. DePaola, M. A. Gimbrone Jr, P. F. Davies, and C. F. Dewey Jr, “Vascular endothelium responds to fluid shear stress gradients,” *Arteriosclerosis and Thrombosis: A Journal of Vascular Biology*, vol. 12, no. 11, pp. 1254–1257, 1992.
- [70] J. J. Hathcock, “Flow effects on coagulation and thrombosis,” *Arteriosclerosis, Thrombosis, and Vascular Biology*, vol. 26, no. 8, pp. 1729–1737, 2006.
- [71] X. He and D. N. Ku, “Pulsatile flow in the human left coronary artery bifurcation: average conditions,” *Journal of Biomechanical Engineering*, vol. 118, no. 1, pp. 74–82, 1996.
- [72] D. Giddens, C. Zarins, and S. Glagov, “The role of fluid mechanics in the localization and detection of atherosclerosis,” *Journal of Biomechanical Engineering*, vol. 115, pp. 588–594, 1993.
- [73] M. Jahangiri, M. Saghafian, and M. R. Sadeghi, “Numerical simulation of hemodynamic parameters of turbulent and pulsatile blood flow in flexible artery with single and double stenoses,” *Journal of Mechanical Science and Technology*, vol. 29, no. 8, pp. 3549–3560, 2015.
- [74] D. De Wilde, B. Trachet, G. De Meyer, and P. Segers, “The influence of anesthesia and fluid–structure interaction on simulated shear stress patterns in the carotid bifurcation of mice,” *Journal of Biomechanics*, vol. 49, no. 13, pp. 2741–2747, 2016.
- [75] F. M. A. Box, R. J. van der Geest, M. C. M. Rutten, and J. H. C. Reiber, “The influence of flow, vessel diameter, and non-Newtonian blood viscosity on the wall shear stress in a carotid bifurcation model for unsteady flow,” *Investigative Radiology*, vol. 40, no. 5, pp. 277–294, 2005.
- [76] A. M. Malek, S. L. Alper, and S. Izumo, “Hemodynamic shear stress and its role in atherosclerosis,” *JAMA*, vol. 282, no. 21, pp. 2035–2042, 1999.
- [77] C. Zhang, S. Xie, S. Li et al., “Flow patterns and wall shear stress distribution in human internal carotid arteries: the geometric effect on the risk for stenoses,” *Journal of Biomechanics*, vol. 45, no. 1, pp. 83–89, 2012.
- [78] H. A. Himburg, D. M. Grzybowski, A. L. Hazel, J. A. LaMack, X.-M. Li, and M. H. Friedman, “Spatial comparison between wall shear stress measures and porcine arterial endothelial permeability,” *American Journal of Physiology-Heart and Circulatory Physiology*, vol. 286, no. 5, pp. H1916–H1922, 2004.
- [79] K. P. Papadopoulos, M. Gavaises, I. Pantos, D. G. Katritsis, and N. Mitroglou, “Derivation of flow related risk indices for stenosed left anterior descending coronary arteries with the use of computer simulations,” *Medical Engineering & Physics*, vol. 38, no. 9, pp. 929–939, 2016.
- [80] Z. Chen, H. Yu, Y. Shi et al., “Vascular remodelling relates to an elevated oscillatory shear index and relative residence time in spontaneously hypertensive rats,” *Scientific Reports*, vol. 7, no. 1, pp. 1–10, 2017.